AIAA JOURNAL
Vol. 46, No. 5, May 2008

Aerodynamic Design Optimization Using the Drag-Decomposition Method

Wataru Yamazaki,* Kisa Matsushima,† and Kazuhiro Nakahashi‡
Tohoku University, Sendai 980-8579, Japan

DOI: 10.2514/1.30342

An advanced drag-prediction method, the midfield drag-decomposition method, is applied in aerodynamic design optimization problems. The drag-decomposition method decomposes total drag into wave, profile, and induced and spurious drag components, the latter resulting from the effect of numerical diffusion included in computational fluid dynamics results. Hence, the more accurate drag prediction can be achieved by the elimination of the spurious drag component. In this paper, this method is applied in airfoil, planform, and winglet design optimizations. A conventional genetic algorithm is used as the optimizer. The results showed that the optimizations based on the drag-decomposition method were reliable and efficient. Moreover, detailed information of the drag-reduction mechanisms could be extracted by the drag-component-based investigations.

Nomenclature

a	=	sonic speed
C_D, C_d	=	drag coefficients
C_L, C_l	=	lift coefficients
C_p	=	pressure coefficient
$\boldsymbol{D}$	=	drag force
$\boldsymbol{F}_{(\Delta s,\Delta H)}$	=	entropy and enthalpy drag vector
$\boldsymbol{F}_{\text{induced}}$	=	induced-drag vector
k	=	form factor
M	=	Mach number
$\boldsymbol{n}$	=	outward unit normal vector to a surface, (n_x, n_y, n_z)
P	=	pressure
R	=	gas constant
S_{body}	=	aircraft surface
S_{ref}	=	reference area
S_{wake}	=	wake plane normal to the freestream flow direction
S_∞	=	closed boundary surface of $\boldsymbol{V}$
t/c	=	nondimensional thickness of the airfoil
$\boldsymbol{u}$	=	velocity vector, (u_x, u_y, u_z)
$\boldsymbol{u}_\infty$	=	freestream velocity vector, $(U_\infty, 0, 0)$
$\boldsymbol{V}$	=	flowfield around the aircraft
γ	=	specific heat ratio
Δ	=	perturbation term
ΔH	=	stagnation enthalpy variation
Δs	=	entropy variation
$\Delta\boldsymbol{u}$	=	perturbation velocity vector, $(\Delta u_x, \Delta u_y, \Delta u_z)$
μ_l	=	laminar viscosity coefficient
μ_t	=	eddy viscosity coefficient
ρ	=	density
$\boldsymbol{\tau}$	=	stress tensor, $(\tau_x, \tau_y, \tau_z)^T$

Subscripts

x, y, z	=	orthogonal coordinate system with x axis points to the freestream flow direction
∞	=	freestream value

I. Introduction

THE lift and drag of an aircraft in the cruising condition are known to be the most important parameters for aerodynamic design. Recently, owing to advances in numerical schemes and the rapid development of the computing power, computational fluid dynamics (CFD) has achieved significant progress. However, accurate drag prediction in CFD is still one of the major challenges today, as was pointed out at the AIAA Drag Prediction Workshops [1,2]. In fact, the drag-prediction accuracy within one drag count (1 count $= 1 \times 10^{-4}$, about 0.4% in total drag of a typical transonic aircraft) has still not been achieved. As one of the major bottlenecks, the effect of computational mesh dependency is pointed out.

Traditionally, *surface integration*, or the *near-field method*, is used for the drag prediction in CFD computations. In this method, the pressure and stress tensor on the surface of the aircraft body are integrated for the drag prediction. However, it has been pointed out that the total drag computed by the near-field method includes inaccuracies relating to numerical diffusion and errors, and such inaccuracies cannot be isolated from the total drag. Recently, two advanced drag-prediction methods based on the theory of momentum conservation around an aircraft have attracted much attention. One is called *wake integration*, or the *far-field method* [3–5], which can compute drag components from the surface integration on a wake plane. The other is called *flowfield integration*, or the *midfield method* [2,6–9], which can compute drag components from the volume integration around the aircraft and is derived from the far-field method by applying the divergence theorem, also known as Gauss's theorem. In the midfield method, the spurious drag component, which is based on the spurious entropy production due to numerical diffusion, can be computed and isolated from the total drag; this should enable more accurate drag prediction.

Other advantages of the midfield method are that it enables the drag to be decomposed and visualized. By using the midfield method, the total drag can be decomposed into three physical components of wave, profile and induced drag, and one spurious drag component. In Fig. 1, the classification of these drag components is summarized. (Note that in this paper, the profile drag is defined as a drag component based on the entropy production due to the effect of the boundary layer and wake). Moreover, the local drag amount and the generated positions can be visualized in the flowfield, because the integrand of the volume integral formula indicates the drag

Presented as Paper 2006-3332 at the 24th AIAA Applied Aerodynamics Conference, San Francisco, CA, 5–8 June 2006; received 8 February 2007; revision received 13 October 2007; accepted for publication 15 November 2007.

*Ph.D. Student, Department of Aerospace Engineering; currently Postdoctoral Researcher, Applied Aerodynamics Department, ONERA. Student Member AIAA.

†Associated Professor, Department of Aerospace Engineering. Senior Member AIAA.

‡Professor, Department of Aerospace Engineering. Associate Fellow AIAA.

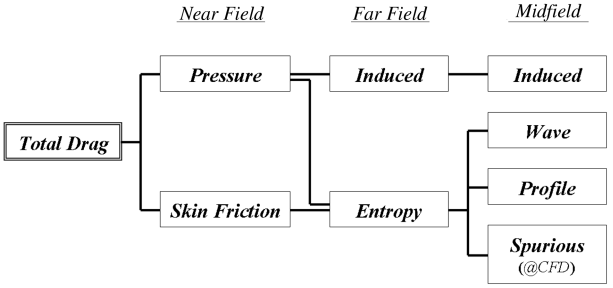

Fig. 1 Drag components and the classification.

production rate per unit volume. By using these abilities, the drag-reduction mechanisms achieved in design optimizations can be discussed in detail.

Recently, aerodynamic design optimizations using CFD computations with optimization algorithms are widely conducted in many laboratories and industries. In such research, coarse computational meshes are usually used for the aerodynamic evaluation to reduce the total computational cost of the optimization. It implies that the total drag computed by the coarse mesh, which is usually used as one of the objective functions, includes a significant percentage of spurious drag due to the mesh coarseness. Actually, the drag-decomposition method was applied to the initial and optimal designs obtained in an aerodynamic design optimization that minimized the total drag. As a result, reduction of not only the physical drag components, but also the spurious drag component, was confirmed in the optimal design [9]. It means that optimizations minimizing the total drag have the risk that they may reduce the spurious drag (they may reduce only the spurious drag at the worst case) in the optimization process. It will cause some inefficiency in the design optimizations and will affect the result of the optimizations. Therefore, aerodynamic optimizations based on the physical drag components will increase the efficiency and reliability. In addition, more meaningful design optimizations will be achieved by the multi-objective minimization of each physical drag component.

In this paper, therefore, the midfield drag-decomposition method is applied in aerodynamic design optimization problems, then its capability, validity, and effectiveness are analyzed in detail.

II. Drag-Decomposition Methods

This section outlines the concept and computational method of the three drag-prediction methods.

A. Near-Field Method (Surface Integration)

In the near-field method, the drag force is computed as follows:

$$D = \iint_{S_{\text{body}}} [-(P - P_\infty)n_x + \tau_x \cdot \boldsymbol{n}]\,\mathrm{d}s \tag{1}$$

where S_{body} indicates the surface of the aircraft, and the first and second terms correspond to the pressure drag component and skin-friction drag component, respectively.

B. Far-Field Method (Wake Integration)

In the drag-prediction method based on the theory of momentum conservation, the drag force is computed as follows:

$$D = \iint_{S_\infty} [-\rho(u_x - U_\infty)(\boldsymbol{u}\cdot\boldsymbol{n}) - (P - P_\infty)n_x + \tau_x \cdot \boldsymbol{n}]\,\mathrm{d}s \tag{2}$$

where S_∞ indicates an arbitrary closed surface around the aircraft. It was demonstrated that Eq. (2) can be transformed as follows by using the small-perturbation approximation [3]:

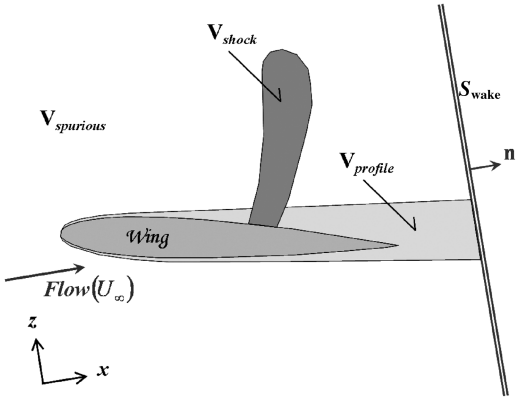

Fig. 2 Schematic sketch for the far- and midfield methods.

$$\begin{aligned} D &= \iint_{S_{\text{wake}}} P_\infty \frac{\Delta s}{R}\,\mathrm{d}s - \iint_{S_{\text{wake}}} \rho_\infty \Delta H\,\mathrm{d}s \\ &\quad + \iint_{S_{\text{wake}}} \boldsymbol{F}_{\text{induced}} \cdot \boldsymbol{n}\,\mathrm{d}s + \mathcal{O}(\Delta^2) \\ \boldsymbol{F}_{\text{induced}} &= \begin{pmatrix} \frac{\rho_\infty}{2}[(\Delta u_y^2 + \Delta u_z^2) - (1 - M_\infty^2)\Delta u_x^2] \\ -\rho_\infty \Delta u_y \Delta u_x \\ -\rho_\infty \Delta u_z \Delta u_x \end{pmatrix}^T \end{aligned} \tag{3}$$

where S_{wake} indicates a wake plane normal to the freestream flow direction, as shown schematically in Fig. 2. The first term of Eq. (3) corresponds to entropy drag, which includes the wave, profile, and spurious drag components. The second term including ΔH can be neglected in cases in which external work is not supplied in flow. The third term including $\boldsymbol{F}_{\text{induced}}$ is based on the vorticity, which corresponds to the induced drag.

C. Midfield Method (Flowfield Integration)

As mentioned earlier, the midfield method is derived from the far-field method by applying the divergence theorem, also known as Gauss's theorem. First, the concept is explained using the entropy and enthalpy terms. By using the divergence theorem, the entropy and enthalpy terms of the far-field method can be transformed as follows:

$$\begin{aligned} D_{(\Delta s,\Delta H)} &= \iint_{S_{\text{wake}}} \boldsymbol{F}_{(\Delta s,\Delta H)} \cdot \boldsymbol{n}\,\mathrm{d}s \cong \iint_{S_\infty} \boldsymbol{F}_{(\Delta s,\Delta H)} \cdot \boldsymbol{n}\,\mathrm{d}s \\ &= \iiint_V \nabla \cdot \boldsymbol{F}_{(\Delta s,\Delta H)}\,\mathrm{d}v \end{aligned} \tag{4}$$

where $\boldsymbol{V}$ indicates the flowfield around the aircraft, and thus S_∞ indicates the closed boundary surface of $\boldsymbol{V}$. In other words, S_∞ consists of the wake plane of S_{wake} and the far-field surfaces of the upstream/lateral regions. $\boldsymbol{F}_{(\Delta s,\Delta H)}$ is the entropy and enthalpy drag vector, which is defined in [6] as follows:

$$\begin{aligned} \boldsymbol{F}_{(\Delta s,\Delta H)} &= -\rho \Delta \bar{u} \boldsymbol{u} \\ \Delta \bar{u} &= U_\infty \sqrt{1 + \frac{2\Delta H}{U_\infty^2} - \frac{2[e^{(\gamma-1/\gamma)(\Delta s/R)} - 1]}{(\gamma - 1)M_\infty^2}} - U_\infty \end{aligned} \tag{5}$$

where $\Delta\bar{u}$ of Eq. (5) can be expanded in Taylor's series as follows:

$$\begin{aligned} \frac{\Delta \bar{u}}{U_\infty} &= f_{s1}\frac{\Delta s}{R} + f_{s2}\left(\frac{\Delta s}{R}\right)^2 + f_{H1}\frac{\Delta H}{U_\infty^2} + f_{H2}\left(\frac{\Delta H}{U_\infty^2}\right)^2 \\ &\quad + f_{sH2}\frac{\Delta s}{R}\frac{\Delta H}{U_\infty^2} + \mathcal{O}(\Delta^3) \end{aligned} \tag{6}$$

where

$$f_{s1} = -\frac{1}{\gamma M_\infty^2}, \qquad f_{s2} = -\frac{1 + (\gamma - 1)M_\infty^2}{2\gamma^2 M_\infty^4}, \qquad \ldots \tag{7}$$

Now calculate the first-order term of entropy variation as follows:

$$\boldsymbol{F}_{\Delta s1} = \frac{U_\infty}{\gamma M_\infty^2}\frac{\Delta s}{R}\rho \boldsymbol{u} \tag{8}$$

Equation (8) is the well-known Oswatitsch formula. By using Eq. (8) and the small-perturbation approximation, Eq. (4) can be rewritten as follows:

$$D_{\text{entropy}} = \iint_{S_\infty} \frac{P_\infty}{\rho_\infty U_\infty}\frac{\Delta s}{R}(\rho_\infty + \Delta\rho)(\boldsymbol{u}_\infty + \Delta\mathbf{u})\boldsymbol{n}\,\mathrm{d}s \cong \iint_{S_{\text{wake}}} P_\infty \frac{\Delta s}{R}\,\mathrm{d}s \tag{9}$$

Equation (9) is the first term of Eq. (3).

By the transformation to the volume integral form, further drag decomposition of the entropy drag term is possible by the domain decomposition of the flowfield $\boldsymbol{V}$. Physically, entropy variation in the flowfield should originate in the shock ($\boldsymbol{V}_{\text{shock}}$) and wake/boundary-layer region ($\boldsymbol{V}_{\text{profile}}$), and so the entropy variation in the remaining region ($\boldsymbol{V}_{\text{spurious}}$) is considered as an unphysical (spurious) phenomenon. The domain decomposition of the flowfield is shown schematically in Fig. 2. Then Eq. (4) can be transformed as follows:

$$D_{(\Delta s,\Delta H)} = \iiint_{V_{\text{shock}}} \nabla\cdot\boldsymbol{F}_{(\Delta s,\Delta H)}\,\mathrm{d}v + \iiint_{V_{\text{profile}}} \nabla\cdot\boldsymbol{F}_{(\Delta s,\Delta H)}\,\mathrm{d}v + \iiint_{V_{\text{spurious}}} \nabla\cdot\boldsymbol{F}_{(\Delta s,\Delta H)}\,\mathrm{d}v = D_{\text{wave}} + D_{\text{profile}} + D_{\text{spurious}} \tag{10}$$

where D_{wave}, D_{profile}, and D_{spurious} correspond to the wave, profile, and spurious drag components, respectively. Moreover, we can evaluate each drag component as well as the flux computation by using the divergence theorem again as follows (only the formula for wave drag is described):

$$D_{\text{wave}} = \iiint_{V_{\text{shock}}} \nabla\cdot\boldsymbol{F}_{(\Delta s,\Delta H)}\,\mathrm{d}v = \iint_{S_{\text{shock}}} \boldsymbol{F}_{(\Delta s,\Delta H)}\cdot\boldsymbol{n}\,\mathrm{d}s \tag{11}$$

where S_{shock} indicates the boundary surface of $\boldsymbol{V}_{\text{shock}}$. As the reader can guess, spurious entropy drag may be generated in the shock and profile region, and the effect cannot be isolated in this approach. However, it is known that the majority of the spurious drag is generated in a region around the leading edge that is outside of the profile (boundary-layer) region. So the spurious drag generated in the shock and profile region is insignificant. The advantages of the midfield method are that it can divide the entropy drag into the wave, profile, and spurious drag components, and it can visualize the drag amount and generated positions in the flowfield, because the integrand of the volume integral form indicates the drag production rate per unit volume.

The domain decomposition of the flowfield is conducted based on the following shock and profile detection functions. For the detection of the shock region, the following function is used [10]:

$$f_{\text{shock}} = (\boldsymbol{u}\cdot\nabla P)/(a|\nabla P|) \tag{12}$$

For the detection of the wake and boundary-layer regions, the following function is used [7]:

$$f_{\text{profile}} = (\mu_l + \mu_t)/(\mu_l) \tag{13}$$

The regions that satisfy $f_{\text{shock}} \geq 1$ and $f_{\text{profile}} \geq C_{\text{profile}}\cdot(f_{\text{profile}})_\infty$ are recognized as the upstream region of shock waves and the profile region, respectively. C_{profile} is a cutoff value for selecting the profile region, and $C_{\text{profile}} = 1.1$ is used in this research. Although several parameters are required in this domain decomposition process, they are almost insensitive to the results of the drag decomposition [7].

The induced drag can be evaluated in the same manner with Eq. (11) as follows:

$$D_{\text{induced}} = \iint_{S_{\text{wake}}} \boldsymbol{F}_{\text{induced}}\cdot\boldsymbol{n}\,\mathrm{d}s \cong \iint_{S_\infty} \boldsymbol{F}_{\text{induced}}\cdot\boldsymbol{n}\,\mathrm{d}s \tag{14}$$

This formula can be obtained from the third term of Eq. (3).

III. Optimizer and Flow Solvers

In aerodynamic design optimizations, the nonlinearity of the objective functions must be taken into consideration. The applicability to multi-objective design optimizations in which there are several conflicting objective functions is indispensable for practical applications. In this research, an in-house code of a conventional real-coded multi-objective genetic algorithm is adopted as the optimizer, because of the capability for global searching and the applicability to multi-objective optimizations. It is a population-based optimization method simulating the evolutional process of creatures. The population evolves over generations to minimize/maximize the objective functions by the operations of selection, crossover, and mutation [11].

In this research, both structured and unstructured-mesh methods are used for flow computations. The two-dimensional flowfield around airfoils is analyzed by the structured-mesh method. In the computation, compressible thin-layer Navier–Stokes (NS) equations are solved on a C-type mesh. In space, the viscous diffusion terms are discretized by the central-difference approximation. For the convection terms, the third-order monotone upstream-centered schemes for conservation laws (MUSCL) type of total-variation-diminishing scheme is used. In time, the lower–upper symmetric Gauss–Seidel (LU-SGS) implicit method [12] is used for the time integration. The Baldwin–Lomax algebraic model [13] is adopted to treat turbulent boundary layers, and fully turbulent flow is assumed.

Three-dimensional flows around wings and aircraft are analyzed by using an unstructured-mesh CFD solver of Tohoku University aerodynamic simulation (TAS) code [14]. Compressible Euler/NS equations are solved by a finite volume cell-vertex scheme. The numerical flux normal to the control volume boundary is computed using an approximate Riemann solver of Harten–Lax–van-Leer–Einfelds–Wada (HLLEW) [12]. The second-order spatial accuracy is realized by a linear reconstruction of the primitive gas-dynamic variables inside the control volume with Venkatakrishnan's limiter [15]. The LU-SGS implicit method for unstructured meshes [16] is used for the time integration. The original Spalart–Allmaras model [17] is adopted to treat turbulent boundary layers, and fully turbulent flow is assumed.

IV. Validation of Drag-Decomposition Method

In this section, the unstructured-mesh computational results of the subject of the second AIAA Drag Prediction Workshop are analyzed by the drag-decomposition method to present the validity. The drag polar of the DLR-F6 wing–body configuration was computed under the condition of the Mach number of 0.75 and the Reynolds number of 3×10^6. The coarse and medium-size unstructured meshes, which were provided as the official meshes for the second Drag Prediction Workshop [18], were used in the computations. The numbers of mesh points of the coarse and medium meshes were about 1 and 3 million, respectively.

In Fig. 3, the unstructured coarse mesh and surface pressure at the angle of attack of 0.49 deg are visualized. The results of drag decomposition are shown in Figs. 4 and 5. In Fig. 4, the structured-mesh CFD results in the elsA code [2] are also plotted. It was confirmed that the wave, profile, and induced-drag components of the coarse and medium meshes showed good agreement. In addition, they showed good agreement with the results of the elsA code. Only the spurious drag component was reduced with the increase of the mesh resolution. In Fig. 5, the near-field and midfield drag predictions are plotted with the experimental data [1]. In this figure, the prefixes NF and MF represent the near-field and midfield drag predictions, respectively. The midfield-pure-drag plots indicate the sum of the physical drag components (wave plus profile plus induced drag): in other words, the remainder after subtracting the spurious

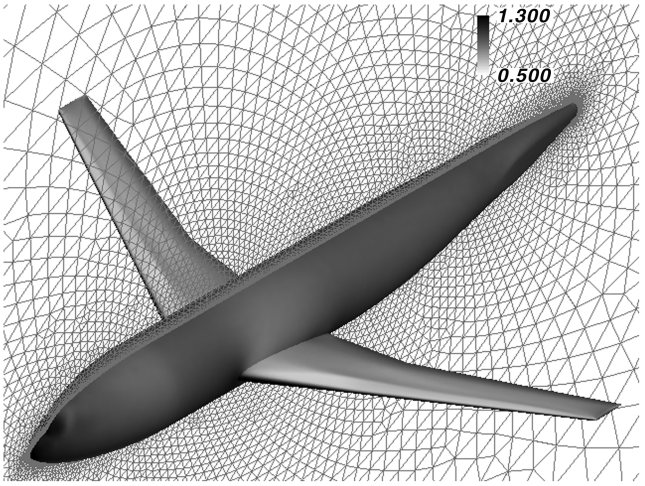

Fig. 3 Mesh and pressure visualization of the DLR-F6.

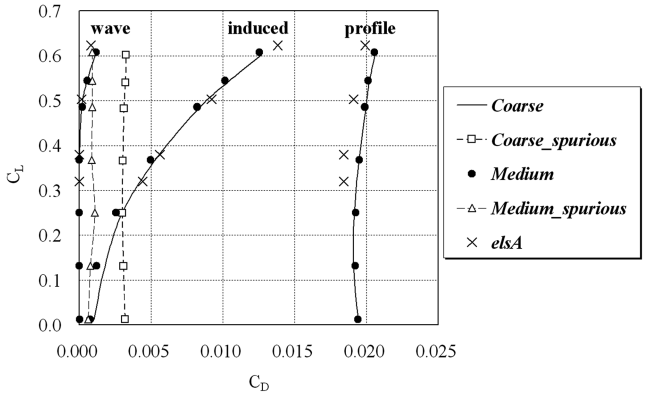

Fig. 4 Drag-decomposition results of the DLR-F6 wing–body configuration.

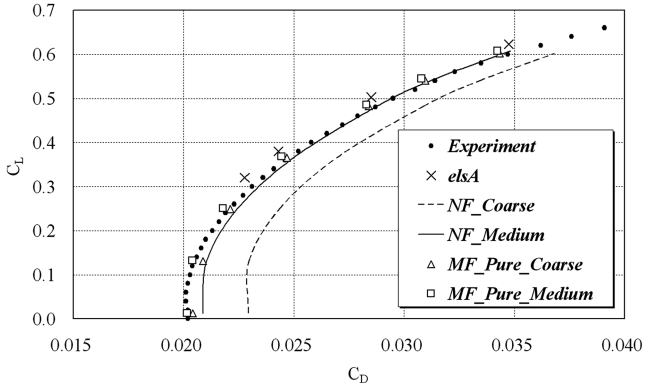

Fig. 5 Pure-drag-prediction results of the DLR-F6 wing–body configuration.

drag from the total drag. The pure drag of both meshes showed good agreement with the experimental data, whereas the total drag of the coarse mesh showed about a 30-count overestimation. This was the spurious drag due to the mesh coarseness. This result showed that more accurate drag prediction could be achieved by using the midfield drag decomposition. In addition, this result showed that the physical drag components could be predicted independently of the mesh resolution by using the drag-decomposition method.

In Fig. 6, the flowfield visualizations at the angle of attack of 0.49 deg and 33% semispan section are shown. The production of entropy drag at the leading/trailing edge, boundary layer, shock positions, and wake region was confirmed. The spurious drag was

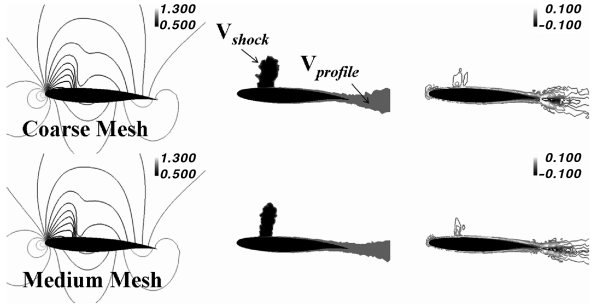

Fig. 6 Flowfield visualization at 33% semispan section of the DLR-F6, from left to right: pressure, domain decomposition, and entropy drag distribution [$\nabla \cdot F_{(\Delta s, \Delta H)}$].

mainly generated around the leading edge and was caused by the numerical diffusion relating to the mesh coarseness. It was also confirmed that the spurious entropy drag production around the leading edge was reduced with the increase of the mesh resolution.

V. Two-Dimensional Airfoil Design Optimization

In this section, simple 2D airfoil design optimizations are conducted to validate the effectiveness of the optimization system using the drag decomposition.

A. Geometry Definition

The airfoil shape was defined by parametric section (PARSEC) [19] airfoil parameterization. In the original PARSEC, as shown in Fig. 7, the geometry is described by 11 characteristic parameters of the airfoil, such as the leading-edge radius, positions/curvatures of the upper/lower crest, and so on. In this optimization, for the simplicity of the problem, the thickness of the trailing edge (Δz_{te}) and the position of the trailing edge (z_{te}) were fixed to zero. The total number of design variables was nine.

B. Objectives and Constraints

The following two single-objective optimization problems were executed:

1) Minimize the near-field total drag (pressure plus skin friction).

2) Minimize the midfield pure drag (wave plus profile).

Note that they are not two-objective optimizations, but two single-objective optimizations. The flow condition was the Mach number of 0.8 with the Reynolds number of 9×10^6. The number of nodes of structured meshes used in this optimization was 183×121, which means a coarse-mesh resolution. This intentional coarse-mesh resolution makes the spurious drag appear to be larger in this design optimization.

In this problem, the NACA0012 airfoil was considered as the initial geometry, and a constraint was set that the sectional area of the new airfoil should be greater than that of NACA0012. Moreover, C_l was kept to 0.4 by adjusting the angle of attack during the flow simulation.

C. Results and Discussion

The evolutional computations were conducted by the population size of 16 and the number of generations of 50: that is, 800 flow evaluations in total. The computation was executed by a master–slave type of parallel computing using the NEC SX-7 of the

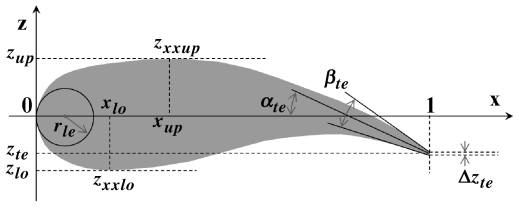

Fig. 7 PARSEC parameterization.

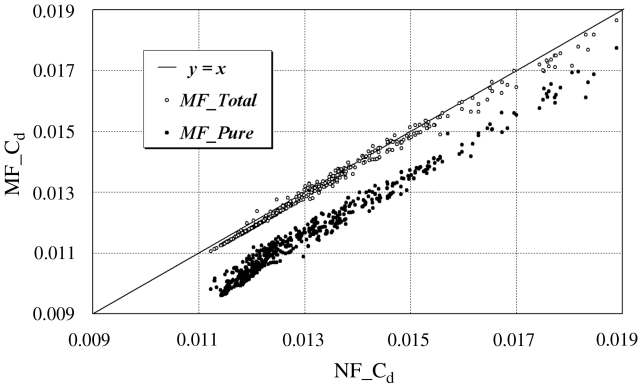

Fig. 8 NF drag vs MF drag in the 2D airfoil design problem.

Information Synergy Center at Tohoku University. The computational time for one generation is about 10 min. The two optimization problems were started from same 16 airfoils that were randomly generated. For the verification of the robustness of the midfield drag prediction, the plot of near-field drag vs midfield drag is shown in Fig. 8. In this figure, all drag values that were predicted in the second optimization problem were indicated. Good agreement between NF and MF total drag was observed. An approximate 10–20-count difference between the total and pure drag was also observed. The histories of the objective functions in each generation are shown in Fig. 9. It was confirmed that the two evolutional optimizations were almost in the convergence states.

In the following discussion, two optimal designs obtained by the two optimization problems were compared. The optimal design of NF_Total optimization and that of MF_Pure were named as optimal designs A and B, respectively (shown in Fig. 9).

The airfoil geometry and C_p distribution of the initial (NACA0012) and two optimal designs are compared in Fig. 10. The geometries of the optimal designs had almost the same features as typical supercritical airfoils. In the C_p distributions of the optimal

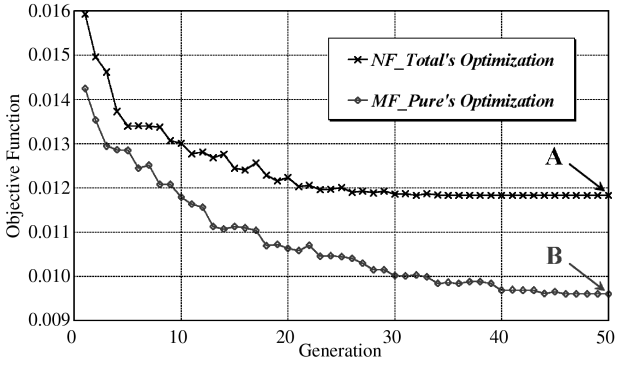

Fig. 9 History of objective functions.

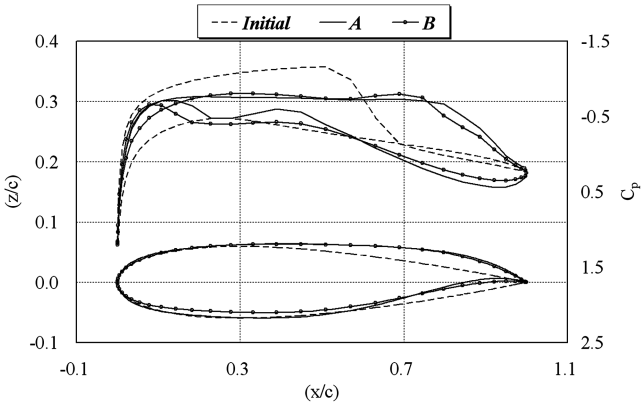

Fig. 10 Comparison of C_p distributions.

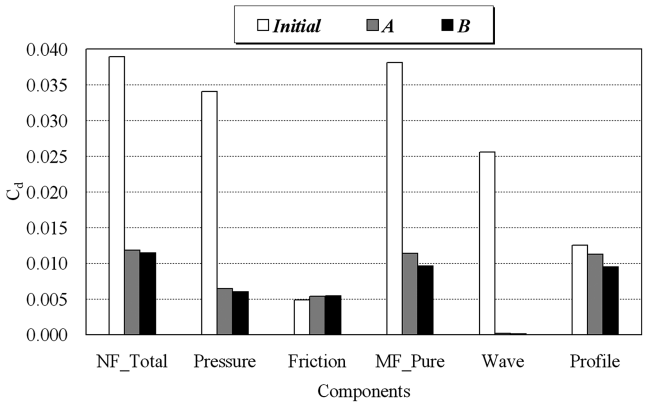

Fig. 11 Behavior of each drag component.

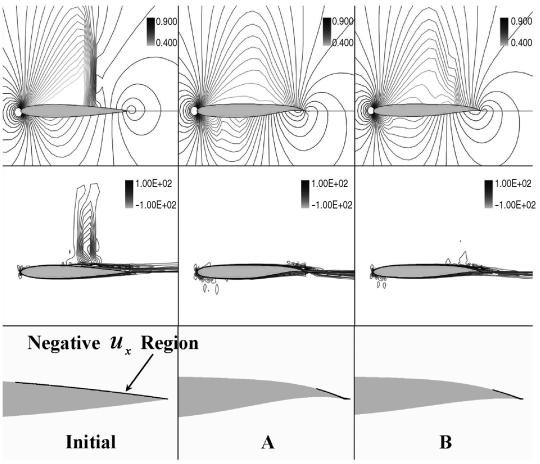

Fig. 12 Flowfield visualizations of initial and optimal designs, from top to bottom: pressure, entropy drag distribution, and separation (negative u_x) region around the trailing edge.

designs, the modification to a rear-loading type and the reduction of the shock strength were confirmed. The behavior of each drag component of the initial and optimal designs is shown in Fig. 11. In the NF drag, the pressure drag was reduced remarkably in both optimal designs, whereas the skin-friction drag was kept almost constant. On the other hand, in the MF drag, the wave drag was reduced remarkably, and the profile drag was also reduced in both optimal designs. In Fig. 12, the flowfield visualizations of the initial and optimal designs are shown. The reduction of the entropy drag due to shock waves was remarkable in both optimal designs. The separation behind the root of the shock wave was absent in both optimal designs, and it contributed to the reduction of the profile drag. This was considered as a secondary product of the reduction of the shock strength.

To validate these designs, fine-mesh computations of the initial and obtained optimal designs were also conducted. The number of mesh points was 323×151. The results of C_p distribution and the behavior of each drag component are shown in Figs. 13 and 14 in the same manner as in Figs. 10 and 11. The wave drag of both optimal designs was increased compared with the coarse-mesh computation. This is due to the better resolution of shock waves by the higher mesh resolution. However, it could be concluded that the tendency of the drag-reduction mechanisms was the same as with the coarse-mesh computations.

In this section, two airfoil design optimizations were conducted by the minimization of total and pure drag, respectively. The optimal designs of A and B showed the same features about the geometry and aerodynamics. This result showed the validity of the optimization system using the midfield drag decomposition. In detail, the optimal design of B showed a better aerodynamic performance than design

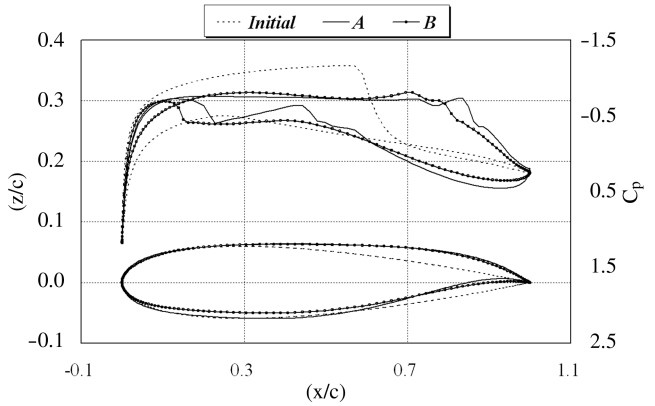

Fig. 13 Comparison of C_p distributions in the fine-mesh computations.

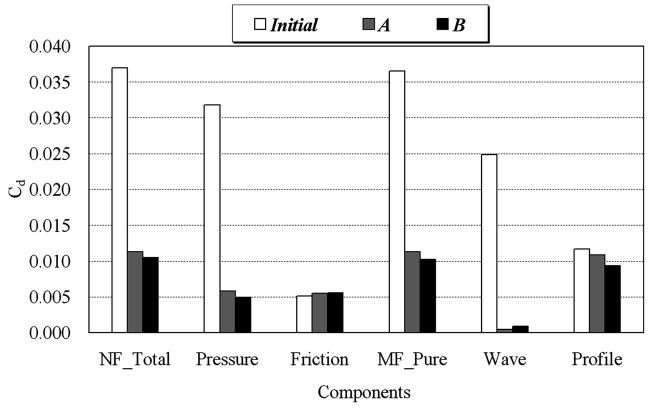

Fig. 14 Behavior of each drag component in the fine-mesh computations.

A, which was thought to be due to the ability of more accurate drag prediction, whereas the optimization by the near-field total drag fell into a local optimal. It meant that more effective and reliable design could be achieved by using the drag-decomposition method.

VI. Planform Design Optimization

In this section, planform shape is designed by the drag-component-based optimization approach, which means the multi-objective optimization of wave and induced-drag components. This optimization is conducted to demonstrate the effectiveness of the optimization system using the drag decomposition.

A. Geometry Definition

The planform shape was defined by seven design variables: the in/outboard spanwise length, in/outboard sweep angle at 25%-chord position, chord length at the kink position, and twist angle at the kink and tip positions, as shown in Fig. 15. The chord length at the root

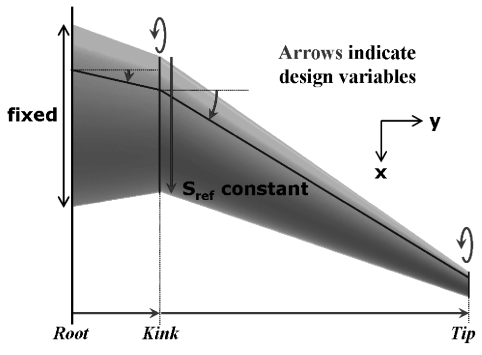

Fig. 15 Planform shape definition.

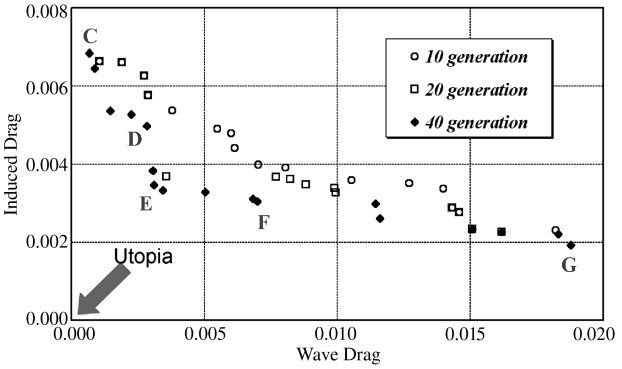

Fig. 16 Information of nondominated solutions in the planform design problem.

position was fixed, and the chord length at the tip position was determined automatically by the rule of the reference area constant. The dihedral angle was kept to 0 deg. In this design, the sectional airfoil shape was fixed to solely investigate the effect of the planform shape parameters. The sectional airfoil shape of all spanwise positions was fixed to a supercritical airfoil with the rule of the t/c constant.

B. Objectives and Constraints

In this optimization, the following multi-objective optimization problem was executed. The first objective was to minimize midfield wave drag. The second objective was to minimize midfield induced drag. The aerodynamic evaluation was conducted by the unstructured-mesh Euler computation. The number of nodes of the unstructured meshes was about $0.2 \sim 0.3$ million, they were generated automatically by the surface mesh generation using an advancing-front approach [20] and by the tetrahedral volume mesh generation using a Delaunay approach [21]. The flow condition was set to the Mach number of 0.84. A constraint was set that the wing volume of new geometry should be greater than a threshold. Moreover, C_L was kept to 0.3 by adjusting the angle of attack.

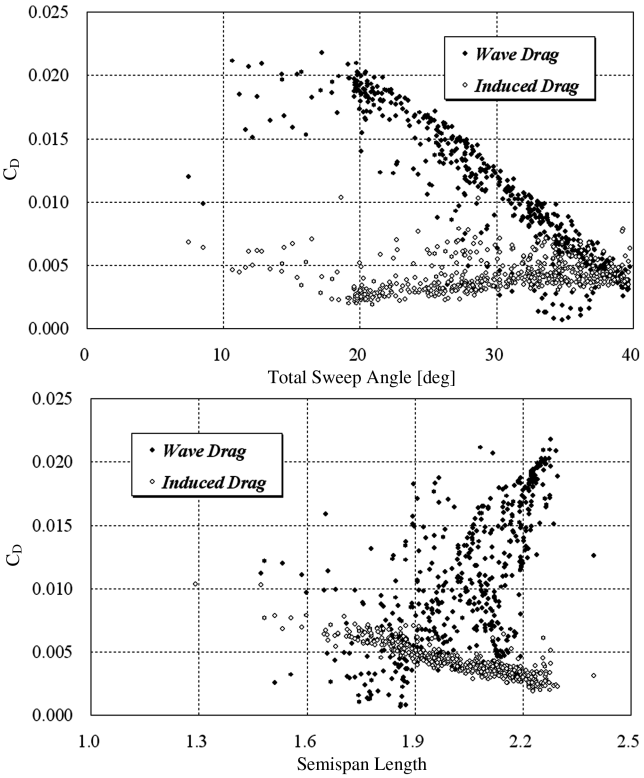

Fig. 17 Relationships between drag components and shape parameters: total sweep angle (top) and semispan length (bottom).

C. Results and Discussion

The evolutional computation was conducted by the population size of 16 and the number of generations of 40: that is, 640 flow evaluations in total. The initial 16 designs were randomly generated, and the computation was executed by a master–slave type of parallel computing. The computational time for one generation is about 3 h in this design problem.

The nondominated-solution information obtained in this optimization is shown in Fig. 16. The tradeoff relationship between the wave and induced-drag component could be captured. In Fig. 17, the relationships between the drag components and shape parameters, which are the total sweep angle and semispan length, are shown. The total sweep angle was defined by connecting the 25%-chord position of the root and wingtip. As the reader could guess, the wave drag had a large dependency on the total sweep angle and was reduced with the increase of sweep angle, whereas the induced drag was almost insensitive to sweep angle. On the other hand, the induced drag was reduced with the increase of the semispan length, which caused the wave drag to be larger. These effects made the tradeoff balance between the wave and induced-drag component. For other design parameters, it is difficult to find some clear relationships with the drag components.

In Fig. 18, the geometries of several nondominated solutions (C–G in Fig. 16) are shown with the surface pressure and shock surfaces. The shock visualization is implemented by using Eq. (12). Designs C, E, and G correspond to the minimized design of wave, pure, and induced drag, respectively. Design C was a daring planform shape with high sweep angle and short chord length at the kink position. The short chord length reduced the expansion regions on the upper side and it reduced the shock waves. From designs C to D to E, the chord length at the kink and the semispan length were gradually increased. At design E, the planform became a conventional geometry with a high sweep angle and high taper ratio. From designs E to F to G, the sweep angle was reduced, whereas the semispan length was increased. In designs F to G, shock waves were generated not only at the upper side, but also at the lower side, with a reduction of the sweep angle. In Fig. 19, the C_p distributions of designs C, E, and G are shown. It was also confirmed that the spanwise lift distribution of design G was very close to the elliptic distribution.

As understood from Fig. 16, the obtained nondominated solutions distributed in the range of 50 counts of the induced drag and 200 counts of the wave drag, respectively. In conventional design optimizations, keeping the lift coefficient constant, the effect of the induced drag tends to be lost by the large influence of the wave drag. However, the current approach made the effect of each drag component clear, so that it could extract much design information.

In Fig. 20, the result of the near-field total drag vs midfield pure drag is shown for all individuals generated in this optimization. The difference between them is about 30 counts or more and is due to the effect of the mesh coarseness and large numerical diffusion of unstructured-mesh computation. In addition, a linear function fitting

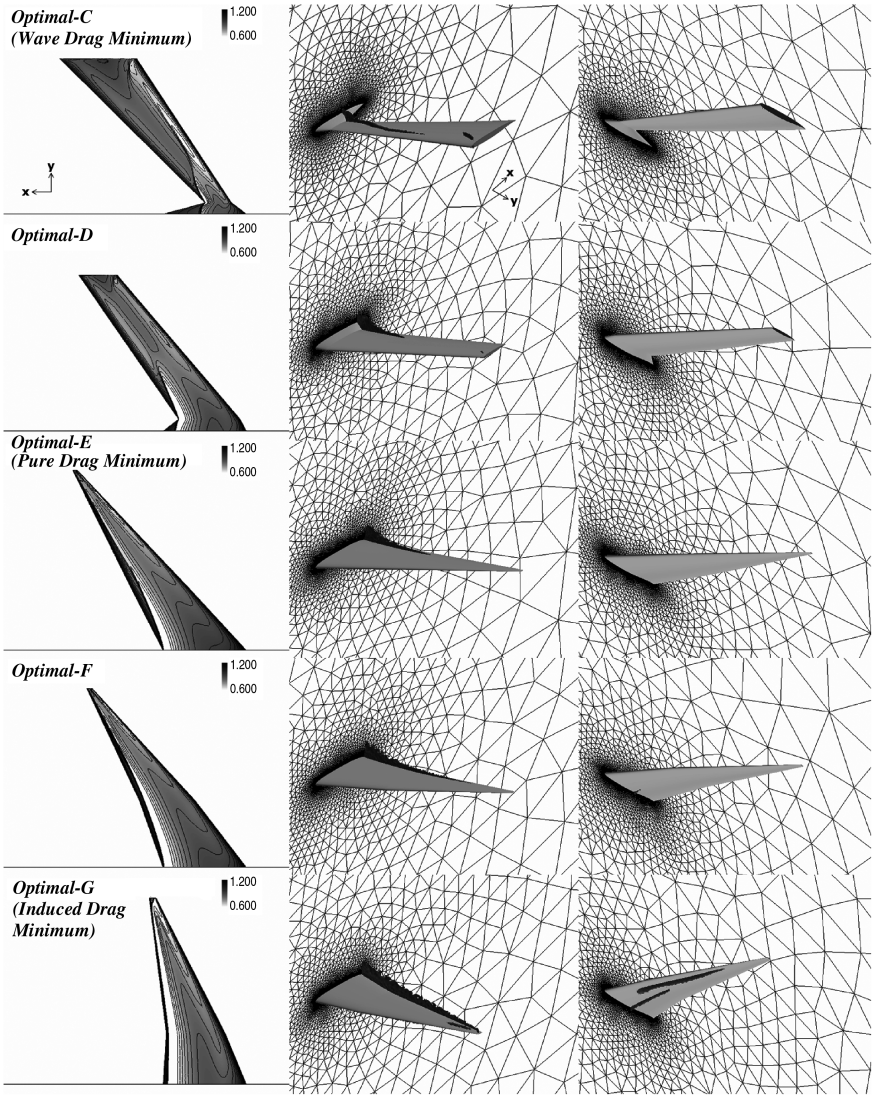

Fig. 18 Visualization of several nondominated solutions, from left to right: pressure on upper surface, shock visualization on upper side, that on lower side.

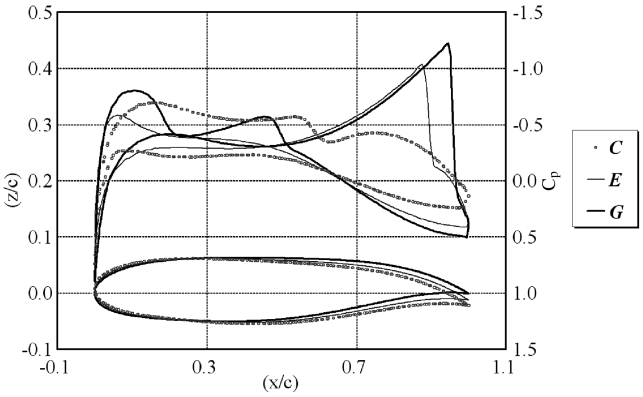

Fig. 19 C_p distributions of representative designs at 30% semispan.

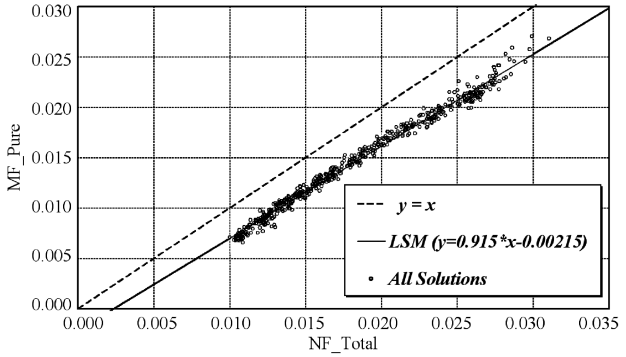

Fig. 20 Near-field total drag vs midfield pure drag.

to the distribution of the pure drag was estimated from the least-squares method. The pure drag distributed around the linear function of the least-squares method with the scatter band of 20 counts or more. This was considered as the uncertainty of the drag prediction using the near-field method.

In this section, the multi-objective optimization of wave and induced-drag component was conducted. The tradeoff information between them was obtained successfully. This result showed that more useful design information could be obtained by using the physical drag components as the objective functions.

VII. Winglet Design Optimization

The advantages of the optimization system using the drag-decomposition method were confirmed in previous sections. In this section, therefore, the optimization system is applied to a more practical design problem: the multi-objective design optimization of winglet shape.

A winglet is a device used to improve the aerodynamic efficiency of aircraft by reducing the lift-induced drag, and it is widely adopted for recent commercial airplanes. Usually, it seems that the aerodynamic improvement by a winglet is within about 10 drag counts. In CFD simulations, especially in unstructured-mesh computations, this order of drag reduction tends to be unclear by the effect of computational mesh dependency. Therefore, accurate drag prediction is essential for the reliable winglet design. Another difficulty of the winglet design is that it includes the variation of each drag component. The equipment of the winglet will cause not only the induced-drag reduction by the increase of the semispan length, but also wave-drag generation at the wing–winglet junction and additional profile drag by the increase of the wetted area. Therefore, the behavior of each drag component has to be discussed in detail for the advanced winglet design.

The drag-decomposition method satisfies these requirements sufficiently. Therefore, the advanced design optimization of a winglet will be realized by using the abilities of the drag-decomposition method.

A. Geometry Definition

As the initial geometry, a DLR-F6 wing–body configuration was used. The winglet shape was defined by five design variables: additional spanwise length b, sweep angle at 25%-chord location Λ, taper ratio λ, cant angle φ, and twist angle θ, as shown in Fig. 21. The section airfoil shape of the winglet was defined by that of the tip section of the DLR-F6 model with the rule of the t/c constant. At the wing–winglet junction region, a simple geometry-smoothing using a quadratic function was given for the preservation of the smoothness around there.

B. Objectives and Constraints

In the design problem of winglet shape, the drag and the bending moment at the wing root position must be taken into consideration simultaneously from the viewpoint of aero/structural dynamics. In the drag evaluation, the increase of the profile drag due to the additional wetted area of the winglet should be considered. For the accurate evaluation of the profile drag component, the Navier–Stokes computation is required, but it makes the computational cost too expensive (10 times or more). In this research, therefore, unstructured Euler computation was used for the flow simulation, and the increase of the profile drag was estimated by a simple algebraic model as follows [22]:

$$\Delta C_{D_{\text{profile}}} = k \cdot \Delta C_{D_{\text{friction}}} = f(\Delta S_{\text{wet}}, \Lambda)$$

$$\Delta C_{D_{\text{friction}}} = \left[\frac{0.455(1+0.15M_\infty^2)^{-0.58}}{(\log_{10} Re)^{2.58}}\right]\frac{\Delta S_{\text{wet}}}{S_{\text{ref}}} \tag{15}$$

$$k = 1 + \frac{2C(t/c)\cos^2\Lambda}{\sqrt{1-M_\infty^2\cos^2\Lambda}} + \frac{C^2\cos^2\Lambda(t/c)^2(1+5\cos^2\Lambda)}{2(1-M_\infty^2\cos^2\Lambda)}$$

where $Re = 3 \times 10^6$, $C = 1.1$, $t/c = 0.12$, ΔS_{wet} is the additional wetted area, and Λ is the sweep angle of the winglet.

The definition of the objective functions was as follows.

1) Minimize pure drag* (wave drag plus induced drag plus $\Delta C_{D_{\text{profile}}}$).

2) Minimize the bending moment of the wing at the wing root position.

The flow condition was set to the Mach number of 0.8. The number of nodes of the unstructured meshes was about 0.4 million. The unstructured meshes with various winglets were generated automatically by using Delaunay approaches [21,23]. As the constraint, C_L was kept to 0.5 by adjusting the angle of attack during the flow simulation.

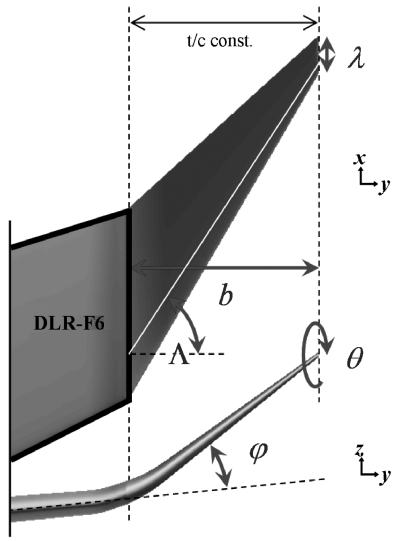

Fig. 21 Winglet shape definition.

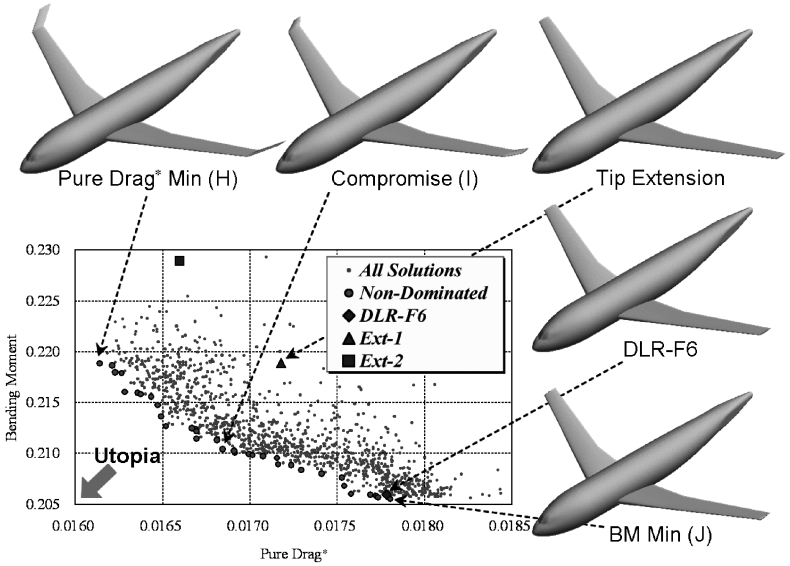

Fig. 22 Information of nondominated solutions in winglet design problem.

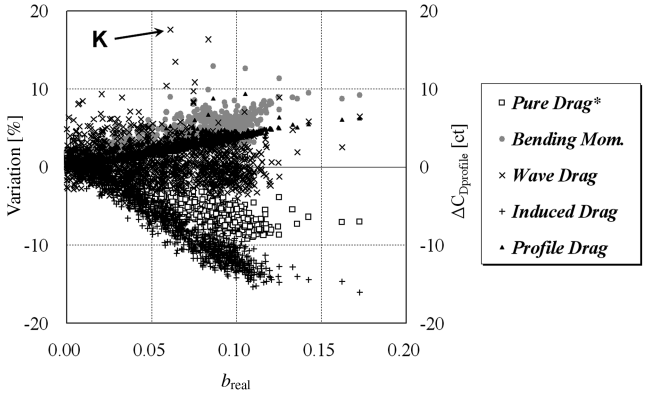

Fig. 23 Relationships between drag/moment and b_{real}.

C. Results and Discussion

The evolutional computation was conducted by the population size of 32 and the number of generations of 20: that is, 640 flow evaluations in total. The initial 32 designs were randomly generated, and the computation was executed by a master–slave type of parallel computing. The computational time for one generation is about 4 h. The nondominated-solution information obtained in this optimization is shown in Fig. 22. In this figure, the geometry of several representative nondominated solutions (H, I, and J), an initial design (DLR-F6), and a simple tip-extension design within the design space (Ext-1) are also indicated. The design J had almost the same performance and geometry as the initial design. The tradeoff relationship between the pure drag* and bending moment was captured successfully. It was also confirmed that the obtained nondominated solutions had a better performance than the simple tip-extension design.

For the analyses of the drag-reduction mechanisms, the drag-component-based investigation was conducted. In Fig. 23, the relationships between the drag/moment and shape parameter b_{real} are shown; b_{real} is defined as the *real* length of winglet as follows:

$$b_{\text{real}} = b/\cos(\Lambda)/\cos(\varphi) \tag{16}$$

The reduction of the induced and pure drag*, and increase of the bending moment and $\Delta C_{D_{\text{profile}}}$ were confirmed with higher b_{real}. These relationships made the tradeoff balance between the pure drag* and bending moment. The wave drag was almost insensitive to the parameter of b_{real}. By checking the designs with higher wave drag (such as design K indicated in Fig. 23), on the other hand, it was confirmed that the wave drag was sensitive to the dihedral angle of winglet. The increase of wave drag with higher dihedral angle was confirmed. This is due to the increase of the compression effect on the upper wing with higher dihedral angle. Much design information about the drag-reduction mechanisms can be extracted by using this drag-component-based investigation. This data mining for the drag-reduction mechanisms is essential for advanced aerodynamic design optimizations.

Another simple tip-extension design (Ext-2), which had same b_{real} as the nondominated design H, was also analyzed and is indicated in Fig. 22. It showed higher bending moment than the nondominated design H. This result showed the effectiveness of the present drag-decomposition-based optimization system. In Fig. 24, the shock surface visualizations of typical designs, including design K and Ext-2, are shown. In this figure, the induced-drag amount is also visualized on a wake plane. In addition, the spanwise lift distributions are compared in Fig. 25. The sectional lift at the wing root was reduced from J to H (with the reduction of pure drag*), whereas that at the wingtip was increased.

In Fig. 26, the behavior of each drag component of the representative designs is shown. The bending moment is also indicated by using the rightmost scale. Keeping the wave drag almost constant, the induced drag was reduced in the nondominated solutions of H and I. The bending-moment minimized design J had almost the same performance as the initial design. To validate the present design optimization, the Navier–Stokes computations of the representative designs and the drag-decomposition analyses were also conducted in the same flow condition. The hybrid meshes were generated by using an advancing-layer approach [24]. The behavior of each drag component is shown in Fig. 27. The wave drag of NS analyses was reduced in all cases compared with that of Euler analyses. This was because the angle of attack was changed to keep the lift coefficient constant, and then the wave drag was shifted in all cases. Although the additional profile drag was simply estimated by an algebraic model in the Euler analyses, the tendency showed good agreement with that of NS analyses. It was confirmed that, in general, these NS analyses showed the same tendency as the Euler computational results of Fig. 26. This result showed the validity of the present winglet design optimization.

VIII. Conclusions

In this research, the midfield drag-decomposition method was applied in aerodynamic design optimizations. The drag-decomposition method has the capability of accurate drag prediction by

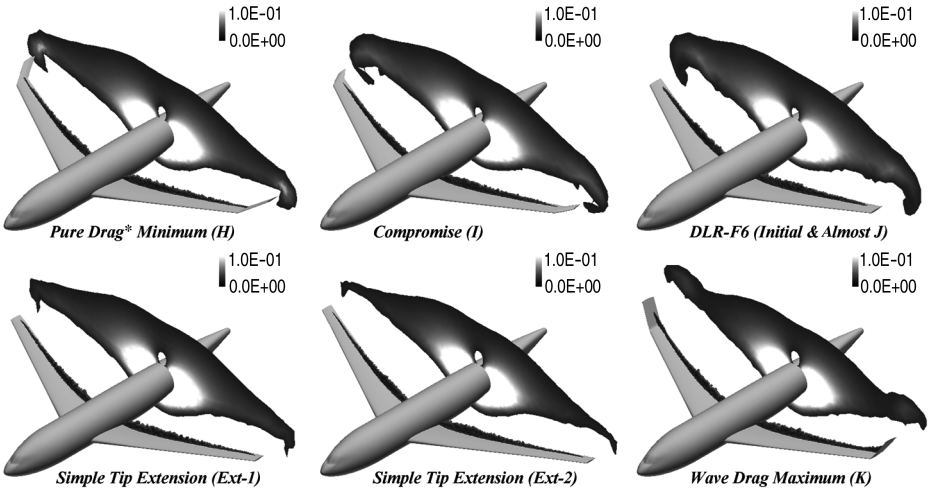

Fig. 24 Shock visualization of typical designs.

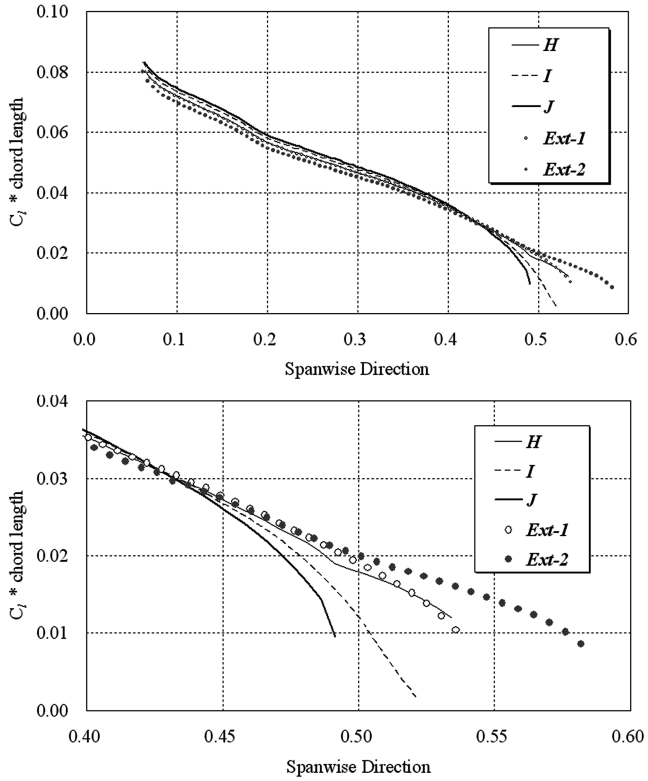

Fig. 25 Spanwise lift distributions: general view (top) and close view around the wingtip (bottom).

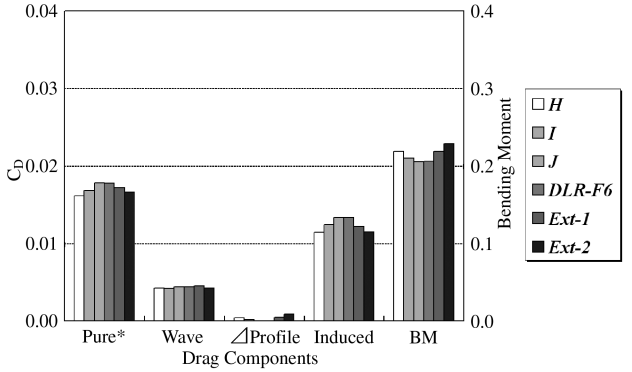

Fig. 26 Behavior of each drag component in the Euler evaluation.

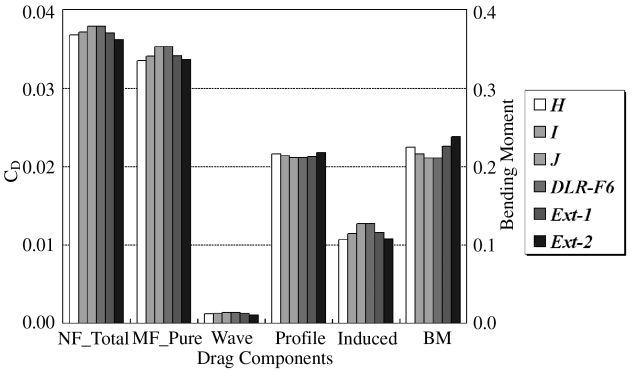

Fig. 27 Behavior of each drag component in the NS evaluation.

excluding the effect of unphysical entropy production, meaningful drag-decomposition, and drag visualization in the flowfield. First, the validity of the drag-decomposition method was investigated. It was shown that more accurate drag prediction was achieved by removing the spurious drag component. Therefore, it was recommended that the midfield physical drag components or the sum of them (pure drag) should be used as objective functions for more efficient and meaningful aerodynamic design optimizations.

To prove the effectiveness of the optimization system, three design optimization problems of the airfoil, planform, and winglet were executed with the drag-decomposition method. The validity and effectiveness of the new optimization system was confirmed in the airfoil design problem. In the planform design, a multi-objective minimization of the wave and induced drag was executed. Then the tradeoff information between the wave and induced drag was obtained successfully. Using the physical drag components as the objective functions enabled obtaining more precise design information. In the winglet design, aiming an application to more practical design, a multi-objective minimization of the drag and bending moment was executed. The tradeoff information between the drag and bending moment was captured successfully. By the drag-component-based investigation, moreover, the drag-reduction mechanisms due to winglet could be analyzed in detail. The induced drag, profile drag, and bending moment had a dependency on the length of winglet, whereas the wave drag had a dependency on the dihedral angle of winglet.

These precise and reliable design optimizations could not have been achieved without the drag-decomposition method. To improve the reliability and efficiency and to extract detailed design information about the drag-reduction mechanisms, the drag-decomposition method is an essential tool in aerodynamic design optimizations.

Acknowledgments

This research was supported by a grant from the Japan Society for the Promotion of Science. The authors would like to thank Kazuhiro Kusunose for his helpful advice. The authors also would like to thank Dimitri Mavriplis for providing the unstructured hybrid meshes of DLR-F6 geometry. The present computation was executed by using the NEC SX-7 of the Information Synergy Center at Tohoku University.

References

[1] Hemsch, M. J., and Morrison, J. H., "Statistical Analysis of CFD Solutions from 2nd Drag Prediction Workshop," AIAA Paper 2004-0556, 2004.

[2] Brodersen, O., Rakowitz, M., Amant, S., Larrieu, P., Destarac, D., and Sutcliffe, M., "Airbus, ONERA, and DLR Results from the 2nd AIAA Drag Prediction Workshop," AIAA Paper 2004-0391, 2004.

[3] Kusunose, K., "A Wake Integration Method for Airplane Drag Prediction," *The 21st Century COE Program International COE of Flow Dynamics Lecture Series*, Vol. 3, Tohoku Univ. Press, Sendai, Japan, 2005, pp. 37–44.

[4] Cummings, R. M., Giles, M. B., and Shrinivas, G. N., "Analysis of the Elements of Drag in Three-Dimensional Viscous and Inviscid Flows," AIAA Paper 1996-2482, 1996.

[5] Van Dam, C. P., "Recent Experience with Different Methods of Drag Prediction," *Progress in Aerospace Sciences*, Vol. 35, No. 8, 1999, pp. 751–798.
doi:10.1016/S0376-0421(99)00009-3

[6] Destarac, D., and Van Der Vooren, J., "Drag/Thrust Analysis of Jet-Propelled Transonic Transport Aircraft; Definition of Physical Drag Components," *Aerospace Science and Technology*, Vol. 8, No. 6, 2004, pp. 545–556.
doi:10.1016/j.ast.2004.03.004

[7] Paparone, L., and Tognaccini, R., "Computational Fluid Dynamics-Based Drag Prediction and Decomposition," *AIAA Journal*, Vol. 41, No. 9, 2003, pp. 1647–1657.

[8] Esquieu, S., "Aircraft Drag Extraction from Patched Grid Computations," AIAA Paper 2003-3659, 2003.

[9] Yamazaki, W., Matsushima, K., and Nakahashi, K., "Application of Drag Decomposition Method to CFD Computational Results," AIAA Paper 2005-4723, 2005.

[10] Lovely, D., and Haimes, R., "Shock Detection from Computational Fluid Dynamics Results," AIAA Paper 1999-3285, 1999.

[11] Fonseca, C. M., and Fleming, P. J., "Genetic Algorithms for Multiobjective Optimization: Formulation, Discussion and Generalization," *Proceedings of the 5th International Conference on Genetic Algorithms*, Morgan Kaufmann, San Francisco, 1993, pp. 416–423.

[12] Obayashi, S., and Guruswamy, G. P., "Convergence Acceleration of a Navier–Stokes Solver for Efficient Static Aeroelastic Computations," *AIAA Journal*, Vol. 33, No. 6, 1995, pp. 1134–1141.

[13] Baldwin, B. S., and Lomax, H., "Thin Layer Approximation and Algebraic Model for Separated Turbulent Flows," AIAA Paper 1978-257, 1978.

[14] Nakahashi, K., Ito, Y., and Togashi, F., "Some Challenges of Realistic Flow Simulations by Unstructured Grid CFD," *International Journal for Numerical Methods in Fluids*, Vol. 43, Nos. 6–7, 2003, pp. 769–783.
doi:10.1002/fld.559

[15] Venkatakrishnan, V., "On the Accuracy of Limiters and Convergence to Steady State Solutions," AIAA Paper 93-0880, 1993.

[16] Sharov, D., and Nakahashi, K., "Reordering of Hybrid Unstructured Grids for Lower–Upper Symmetric Gauss–Seidel Computations," *AIAA Journal*, Vol. 36, No. 3, 1998, pp. 484–486.

[17] Spalart, P. R., and Allmaras, S. R., "A One-Equation Turbulence Model for Aerodynamic Flows," AIAA Paper 92-0439, 1992.

[18] Lee-Rausch, E. M., Frink, N. T., Mavriplis, D. J., Rausch, R. D., and Milholen, W. E., "Transonic Drag Prediction on a DLR-F6 Transport Configuration Using Unstructured Grid Solvers," AIAA Paper 2004-0554, 2004.

[19] Sobieczky, H., "Parametric Airfoils and Wings," Notes on Numerical Fluid Mechanics, Vol. 68, 1998, pp. 71–88.

[20] Ito, Y., and Nakahashi, K., "Direct Surface Triangulation Using Stereolithography Data," *AIAA Journal*, Vol. 40, No. 3, 2002, pp. 490–496.

[21] Sharov, D., and Nakahashi, K., "Hybrid Prismatic/Tetrahedral Grid Generation for Viscous Flow Applications," *AIAA Journal*, Vol. 36, No. 2, 1998, pp. 157–162.

[22] *Aircraft Design: Synthesis and Analysis* [online book], Desktop Aeronautics, Inc., Stanford, CA, http://adg.stanford.edu/aa241/AircraftDesign.html.

[23] Yamazaki, W., "Aerodynamic Optimization of Near-Sonic Plane Based on NEXST-1 SST Model," *Proceedings of the 24th Congress of the International Council of the Aeronautical Sciences* [CD-ROM], Optimage Ltd., Edinburgh, Scotland, U.K., 2004.

[24] Ito, Y., and Nakahashi, K., "Improvements in the Reliability and Quality of Unstructured Hybrid Mesh Generation," *International Journal for Numerical Methods in Fluids*, Vol. 45, No. 1, 2004, pp. 79–108.
doi:10.1002/fld.669

A. Messac
Associate Editor